WELDING RESEARCH

SUPPLEMENT TO THE *WELDING JOURNAL,* JANUARY 2017
Sponsored by the American Welding Society and the Welding Research Council

Fiber Laser Welding of WC-Co and Carbon Steel Dissimilar Materials

This investigation focused on the factors that influence the strength and ductility of dissimilar joints

BY P. XU, D. ZHOU, AND L. LI

ABSTRACT

Welding parameters were investigated for fiber laser welding of cemented carbide WC-Co and steel dissimilar materials. The microstructure, composition, phase, and bend strength of the joints were analyzed using optical metallography, scanning electron microscopy, x-ray diffraction, transmission electron microscopy, and bend testing. The optimized welding parameters included laser power of 2 kW, scanning speed at 0.96 m/min, and heat input of 125 J/mm. The flexural bend strength and yield strength of the joints attained 970 MPa and 876 MPa, much higher than that of conventional brazed joints. The brittle fracture during bending occurred along the fusion boundary and HAZ on the cemented carbide side, where dissolution of WC and penetration of Fe from the fusion zone are believed to have caused embrittlement at the WC-matrix interfaces.

KEYWORDS

• Fiber Laser • Dissimilar Joints • Cemented Carbide • Brittle Fracture

Introduction

Cemented carbide is a composite material of hard carbides and a soft binder metal. The hard carbides include those of Group V and Group VI elements, such as WC, TiC, Mo_2C, TaC_4, Cr_3C_2, VC, and NbC. The soft binder metal is usually cobalt, nickel, iron, or their mixture (Ref. 1). Cemented carbide has been widely used in aerospace, electronics, marine, petrochemical, mining, and automotive industries for decades in engineering applications, such as pipe-valve components, cutting tools, catalytic converters, rock drill tips, and various wear-resistant parts (Refs. 2, 3). Several methods have been used for joining cemented carbide to steel substrates for drill bits and cutting tools. These methods include brazing (Refs. 4–6), sinterbonding (Ref. 7), or diffusion bonding (Refs. 8–10), chemical vapor deposition (Ref. 11), tungsten arc welding (Ref. 12), friction welding (Ref. 13), and, more recently, laser welding (Refs. 14–17).

The challenge in joining cemented carbide and steel dissimilar materials is the low strength and poor ductility of the metallic bond. The strength of brazed joints usually ranges from 150 to 250 MPa (Ref. 5). With special brazing filler metals and pretreatment of cemented carbide, the brazed joint strength can achieve 370 MPa. Okita et al. (Ref. 13) adapted friction welding to join the cemented carbide and steel. A tool steel was friction welded to cemented carbide with an intermediate layer that was dispersion strengthened by tungsten carbide particles in a nickel matrix. The joint tensile strength was found to be greater than 730 MPa when the forge pressure was lower than 250 MPa, but the strength markedly decreased when the forge pressure was greater than 300 MPa.

Tian et al. (Ref. 14) studied dip soldering and welding of carboloy and steel dissimilar materials. Combining laser fusion welding with dip soldering, they found fewer fissures in carboloy, and laser fusion welding could suppress polycrystalline formation in the binding Co, and thus improve the welded joint toughness. Research by Barbatti et al. (Ref. 17) indicated that laser beam welding allowed the successful autogenous joining of a steel to cemented carbide. By welding with a preheating and postweld heat treatment, the temperature gradients were controlled, and lower residual stress level, crack-free, and nonporous, joints were obtained. The mechanical properties of the joints were found to be comparable with those of the conventional brazed steel-cemented carbide joints. Costa et al. (Refs. 15, 16) found the major defects during laser welding

P. XU and D. ZHOU are with Materials Science and Engineering, Shanghai University of Engineering Science, Shanghai, China, and L. LI (leijun@ualberta.ca) *is with Chemical and Materials Engineering, University of Alberta, Edmonton, Canada.*

of WC-12%C cemented carbide to 0.25%C steel to be misalignment, porosity, cracking, and excessive melt-through (for a specimen thickness of 2.5 mm). The horizontal position of the laser beam interaction area was identified to be a major factor for joint quality. The quality was optimized when the laser beam was positioned on the steel side with a distance of 0.2 mm from the bond centerline. If the laser beam interaction area was placed closer to the hard metal, metal cracking was easily observed. However, if the laser beam was positioned farther from the joint (greater than 0.2 mm), the parts did not fully join due to incomplete fusion. The microstructure of the fusion zone was found to be a cellular dendritic structure with an eutectic mixture of austenite and complex carbides occupying the interdendritic spaces of primary austenite dendrites. However, the strength and ductility of laser joints as influenced by dissimilar material welding mechanism have not been studied.

With recent advancements of readily accessible and efficient lasers, especially fiber laser technology, the time has come to make laser welding competitive relative to brazing for achieving strong and possibly ductile joints. This paper provides the results of an investigation into the process parameters for fiber laser welding of WC-20Co to AISI 1045, both popular materials for engineering applications. The focus was on the mechanism for joining and the factors that influence the strength and ductility of the dissimilar joints.

Experimental Procedure

Materials and Welding Procedure

The WC-20Co cemented carbide was used as one of the base materials. The alloy has the following chemical composition: 4.9C, 20Co, and 75.1W (wt-%). A carbon steel, AISI 1045, was used as the other base material. The carbon steel has the following chemical composition: 0.45C, 0.28Si, 0.62Mn, 0.004S, 0.004P, 0.25Cr, 0.25Cu, and balance Fe (wt-%). Disc-shaped base materials with a 50 mm diameter and three thicknesses of 2, 3, and 4 mm were brushed to a 2-μm surface roughness finish. These base metal discs were cut into halves along the diameter and clamped to form a cemented carbide to carbon steel butt joint with no root opening — Fig. 1. A 5-kW maximum output YLS-5000 fiber laser (IPG, USA), with a KR60-HA robot system (Kuka, Germany), and a BIMO QBH laser processing head (HIGHYAG, Germany), was used to weld the butt joint. During the autogenous welding, a copper backing strip was used to support weld root formation. The weld coupons were rigidly clamped to obtain low angular distortions of the joints. The laser beam focal point was varied from 0 mm (on the surface of the plate) with a spot radius of 0.1 to –10 mm defocusing amount. A front and back shielding, provided by gas trailers, was supplied with a high-purity argon gas at a flow rate of 15 to 25 L/min to prevent the molten pool and heat-affected zone (HAZ) from oxidation. The process parameters for laser welding are shown in Table 1. Following welding, the welded joints were evaluated for bead formation, incomplete fusion, microcracking in the fusion zone, or possible liquation cracking in the WC-Co side of the HAZ.

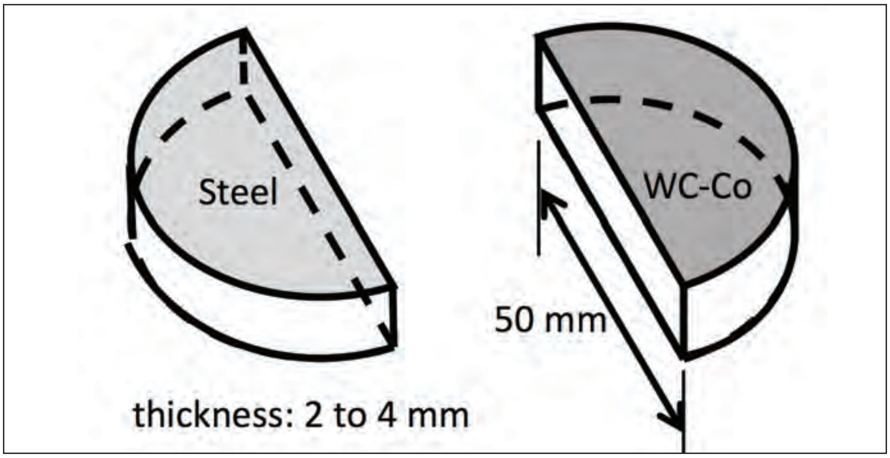

Fig. 1 — Schematic of laser welding specimen.

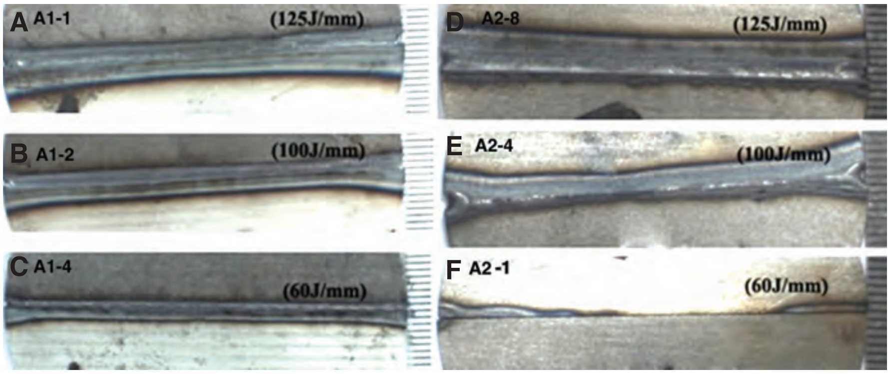

Fig. 2 — Front side weld formation for specimens with preheating. A — A1-1; B — A1-2; C — A1-4; and weld formation for specimens without preheating. D — A2-8; E — A2-4; and F — A2-1.

Bend Test and Microstructure Analysis

Three-point bend strength was measured using a Zwick BTC-T1-FR020TN.A50 universal testing frame (Zwick, Germany) that is stepper motor driven and with a 20-kN load cell. The welded specimens were cut into bend test coupons with dimensions of 48 × 4 × 2 mm (specimens A2-2, A2-8, and A2-9) or 48 × 4 × 3 mm (specimens B3-2). The as-welded surfaces were ground along the longitudinal axis of the test coupons. The length of the three-point bend test span (L) was 36 mm. All coupons were tested in face-bend configuration at ambient

Table 1 — Laser Welding Parameters and Formation of Welds

Specimen	Specimen thickness (mm)	Defocus (mm)	Preheat Laser Power (kW)	Welding Laser Power (kW)	Scan Speed (m/min)	Energy Input (J/mm)	Complete Weld Penetration
A0-1	2	0	0	2.7	1.8	90	No
A0-2	2	0	0	2.7	1.8	90	Yes
A0-3	2	-8	0	2.7	1.8	90	Yes
A0-4	2	-8	0	2.3	1.8	90	Yes
A1-1	2	-8	0.2	2.0	0.96	125	Yes
A1-2	2	-8	0.2	2.0	1.20	100	Yes
A1-3	2	-8	0.2	2.0	1.44	83	Yes
A1-4	2	-8	0.2	2.0	2.00	60	Yes
A1-5	2	-8	0.2	2.0	2.40	50	Yes
A2-1	2	-8	0	1.2	1.20	60	No
A2-2	2	-8	0	1.8	0.84	129	Yes
A2-3	2	-8	0	1.8	0.96	113	Yes
A2-4	2	-8	0	1.8	1.08	100	No
A2-5	2	-8	0	1.8	1.20	90	No
A2-6	2	-8	0	2.0	0.84	143	Yes
A2-7	2	-8	0	2.0	0.90	135	Yes
A2-8	2	-8	0	2.0	0.96	125	Yes
A2-9	2	-8	0	2.0	1.02	118	Yes
B0-1	3	-8	0	3.0	1.20	150	Yes
B0-2	3	-8	0	2.7	1.08	150	No
B1-1	3	-8	0	3.0	1.08	166	Yes
B1-2	3	-8	0	2.7	0.98	166	No
B2-1	3	-8	0	2.7	0.84	192	Yes
B2-2	3	-8	0	2.5	0.78	192	Yes
B3-1	3	-8	0	2.7	0.78	208	Yes
B3-2	3	-8	0	2.5	0.72	208	Yes
C0-1	4	-8	0.5	3.0	1.56	115	No
C0-2	4	-8	0.5	3.5	1.56	135	Yes
C0-3	4	-8	0.5	3.7	1.56	142	Yes

temperature (20°C) at a constant crosshead velocity of 0.05 mm/min with a data acquisition rate of one sample per second. The flexural stress (σ_f) and flexural strain (ε_f) at the outer fiber of the bend coupons are calculated by

$$\sigma_f = \frac{3PL}{2bd^2} \tag{1}$$

and

$$\varepsilon_f = \frac{6\delta d}{L^2} \tag{2}$$

where P is the measured load, L is the support span, b is the width and d is the thickness of the specimen cross-section, and δ is the measured deflection along the loading direction. The flexural yield strength (σ_Y) was determined at the 0.2% strain offset; the flexural bend strength (σ_T) was determined from the peak point of each stress-strain curve.

The microstructure of the laser welds was characterized by x-ray diffraction (XRD), optical metallography, scanning electron microscopy (SEM), and transmission electron microscopy (TEM). The XRD measurements were carried out on weld samples using an X'Pert PRO X-ray diffractometer with a Cu K_a radiation (λ = 0.15406 nm) and a BLK2 cooling cycle system. The scanning step size was 0.026 deg, and the scanning range was 15 to 120 deg continuous. The scanning speed was 0.438 deg/s. For the SEM, the current and voltage were at 40 mA and 40 kV, respectively.

The optical microscopy and SEM specimens were prepared by mounting, grinding and polishing, and etching with the Murakami's reagent (10 g potassium ferricyanide $K_3Fe(CN)_6$, 10 g sodium hydroxide NaOH, and 100 mL water, freshly prepared) (Ref. 27). High-resolution microstructure of the as-welded fusion zone was characterized using a JEM 2010 TEM (JEOL, Japan). Samples for TEM were prepared using ion milling. The TEM parameters were 200-kV acceleration voltage, 96-μA dark current, 128-μA emission current, 109.8-pA/cm^2 current density, 2-s exposure time, and magnifications between 20k and 200k times.

Results

Weld Formation

The weld penetration and bead formation are affected by welding parameters (Table 1). The laser spot position was found to influence the fusion of the dissimilar materials. As the melting point of WC (approx. 2700°C) is much higher than that of carbon steel (approx. 1350°C), the laser spot needs to be located at 1 mm from the butt joint line toward the cemented carbide side. If the laser spot focuses at the steel side (specimen A0-1) or on the butt joint line (specimens A0-2, A0-3, and A0-4), incomplete fusion was shown to have happened on the WC side. Among the welding parameters, the defocusing amount was found to be a sensitive factor to influence the weld formation of WC-20Co cemented carbide to AISI 1045 carbon steel. The results indicated that specimen A0-3 (defocusing amount –8 mm below surface), in contrast with specimen A0-2 (defocusing amount was zero, or on surface), obtained complete joint penetration without weld spatter. Therefore, all subsequent welding trials were conducted with a –8 mm defocused laser spot on the WC-Co side.

Local preheating by a "dry-run" of the laser scan (i.e., all parameters kept the same, except the laser power being reduced to 1/10th of the level for welding) was included in the welding procedure (Table 1). Figure 2 illustrates the influence of preheating on the weld formation during fiber laser welding. The specimens with preheating (specimens A1-1, A1-2, and A1-4) had consistently better penetration than those without preheating (specimens A2-1, A2-4, and A2-8). However, microcracks were observed on the surface of the cemented carbide HAZ if the preheat is combined with an increase of welding heat input (e.g., specimen A1-1).

The relative effect of laser power and scan rate for a constant heat input on weld formation was investigated (Table 1). With a heat input of 150 J/mm, if the laser power is 2.7 kW and scan rate is 1.08 m/min (specimen B0-2), a good weld formation on the front side but a poor penetration of weld bead on the back side were obtained for the 3-mm-thick specimens. While the heat input was kept constant at 150 J/mm, if the laser power was increased to 3.0 kW and scan rate increased to 1.20 m/min (specimen B0-1), complete penetration with good weld formation was obtained. A similar result was obtained for a constant heat input of 166 J/mm. With a laser power of 2.7 kW and scan rate of 0.98 m/min (specimen B1-2), insufficient penetration was observed at the end of the weld; while complete joint penetration was obtained with an increased laser power to 3.0 kW and a increased scan rate of 1.08 m/min (specimen B1-1). These results can be observed in Fig. 3, which shows the weld formation and penetration of specimens B0-1, B0-2, B1-1, and B1-2. Within the range of parameter variations in this study, it seems that for a constant heat input, increasing the laser power has a greater effect than decreasing the laser scan rate, on enhancing the penetration.

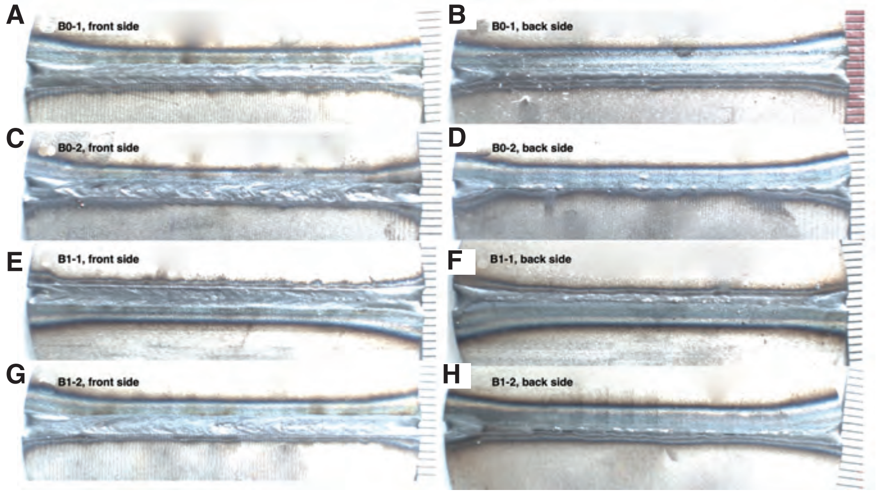

Fig. 3 — Front side weld formation. A — Specimen B0-1; C — Specimen B0-2; E — Specimen B1-1; and G — Specimen B1-2. Back side weld formation. B — Specimen B0-1; D — Specimen B0-2; F — Specimen 1-1; and H — Specimen B1-2.

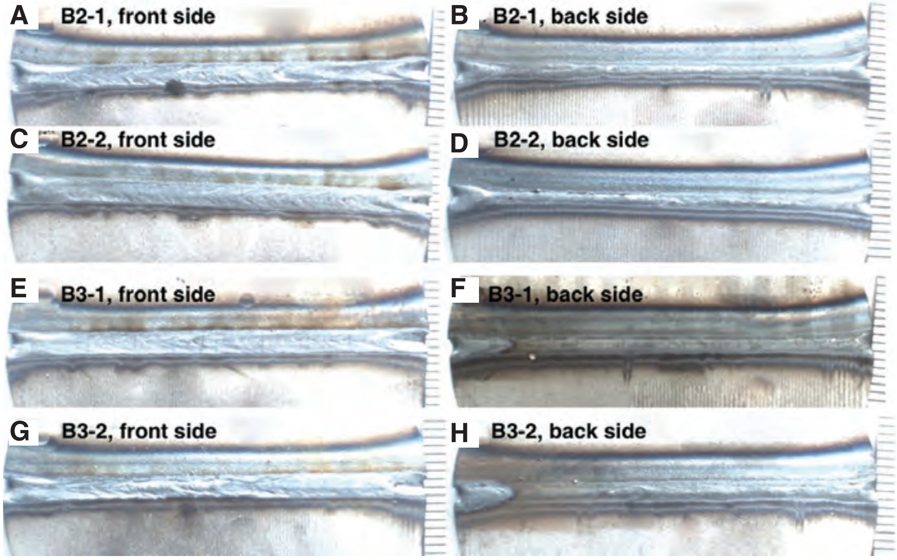

Fig. 4 — Front side weld formation. A — Specimen B2-1; C — Specimen B2-2; E — Specimen B3-1; G — Specimen B3-2. Back side weld formation. B — Specimen B2-1; D — Specimen B2-2; F — Specimen B3-1; H — Specimen B3-2.

Figure 4 shows the changes in weld formation for specimens B2-1, B2-2, B3-1, and B3-2, when the heat input was increased from 192 J/mm to 208 J/mm. The weld widths on the front side are 2.39, 2.18, 2.5, and 2.29 mm, and the widths on the back side are 1.26, 1.38, 1.2, and 1.31 mm, respectively. No cracks were observed in complete-joint-penetration laser welds except on specimen B3-1. Therefore, for 3-mm WC-20Co and AISI 1045 steel laser welding, it is recommended to use a heat input in the range of 192 to 208 J/mm, and a laser power in the range of 2.5 to 2.7 kW.

With the increase of plate thickness to 4 mm, it becomes difficult to join the WC-20Co cemented carbide to AISI 1045 steel using the current welding setup. Poor penetration with

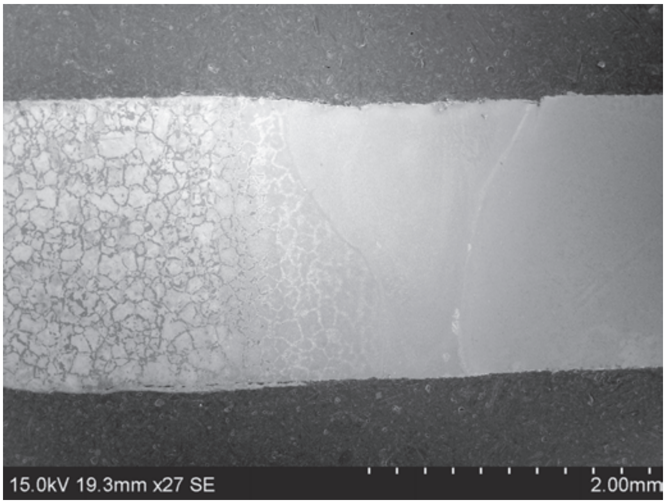

Fig. 5 — Cross-sectional view of a typical joint (A1-1) of AISI 1045 (left side) and WC-Co (right side).

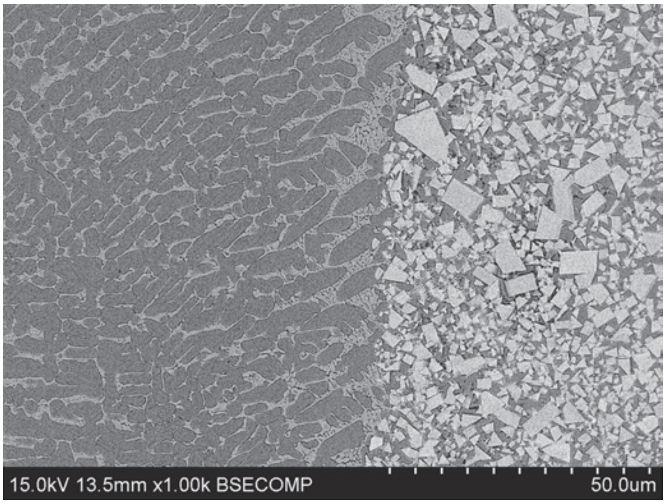

Fig. 6 — Backscattered electron image of a typical joint near the fusion boundary on the WC-Co side.

unacceptable weld formation was obtained if the heat input was below 115 J/mm. When the heat input was increased to above 134 J/mm, not only longitudinal microcracks, but also the transverse microcracks were observed on the surface and cross sections of the laser fusion zones.

Microstructure of Joints

A typical joint has the nail-head shaped autogenous weld fusion zone with a smooth top and root formation — Fig. 5. There is a greater dilution from the steel side than from the WC-Co side. A micrograph of the fusion boundary region on the WC-Co side is shown in Fig. 6. The fusion zone on the left side of the figure appears to have solidified in primary dendritic and eutectic microstructure; the cemented carbide base material on the right side of the figure appears to have retained the cubic and triangular WC particles in the Co matrix. The fusion zone close to the AISI 1045 side fusion boundary also appears to have a primary dendritic and eutectic microstructure, but seems to show an increased size for primary dendrites — Fig. 7. The center of the weld fusion zone shares a similar primary dendritic and eutectic microstructure — Fig. 8. A chemical analysis of the key points in the microstructure revealed the primary dendrites to have the composition of a 0.7 wt-% carbon steel alloyed with 15 wt-% W and 5 wt-% Co (Table 2). It is evident from the dark needles that the steel dendrites may have further transformed to martensite-austenite constituents on-cooling — Fig. 8. The eutectic regions have a typical composition of 50 wt-% Fe, 45 wt-% W, and a relatively higher C concentration; therefore, it is reasonable to suggest one eutectic phase to be *W(Fe)C* carbide (Table 2).

Specimens from the weld fusion zone were analyzed by XRD for crystal structures — Fig. 9. The phases identified in the fusion zone included a-ferrite, martensite, Fe-containing carbides (Fe_3W_3C and Fe_6W_6C), and a small amount of *MC* (*M* being W and Fe) carbide. Due to the overlapping peaks of ferrite and martensite, they remain to be differentiated. However, the high-carbon content in the dendritic regions seems to favor the identification of the peaks due to martensite. If ferrite was present at room temperature for this fusion zone, the extra carbon would have precipitated as carbides, because the solubility of carbon in ferrite was low. There is no evidence of carbides in the primary dendritic regions under the resolution of the BSE micrograph — Fig. 8.

Table 2 — EDS Analysis of Chemical Composition for Locations Labeled in Fig. 8

Point	Carbon (wt-%)(at-%)	Iron (wt-%)(at-%)	Cobalt (wt-%)(at-%)	Tungsten (wt-%)(at-%)
A	(0.61)(3.10)	(78.95)(86.81)	(4.61)(4.81)	(15.83)(5.29)
B	(0.64)(4.20)	(51.61)(73.07)	(2.42)(3.24)	(45.33)(19.49)
C	(0.75)(3.79)	(80.01)(86.51)	(4.86)(4.98)	(14.37)(4.72)

The phases in the fusion boundary and HAZ of the WC-Co base material were identified from XRD of longitudinal specimens extracted parallel to the welds — Fig. 10. The phase composition for the HAZ is similar to that of the weld fusion zone, including a-WC, some eutectic carbides (Fe_3W_3C and Fe_6W_6C), and a weak indiction for a-Fe (ferrite) and martensite. The dominant phase in the HAZ was WC carbide, which was not significant in the fusion zone. It was notable that the Co binding phase (of the HCP crystal structure) in the base material WC-Co was not detected in the HAZ. Significant alterations in the Co binding phase in the WC-Co HAZ must have happened during laser welding.

Bend Strength and Fractography

Due to the statistical nature of mechanical properties of cemented carbides, four repeat specimens were bend-tested for each welded sample. Figure 11 summarizes the flexural stress-flexural strain curves from the three-point bend testing of typical

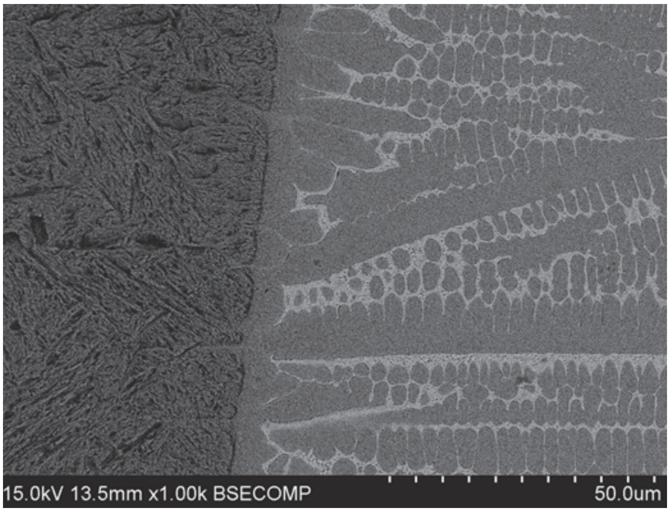

Fig. 7 — Backscattered electron image of a typical joint near the fusion boundary on the AISI 1045 side.

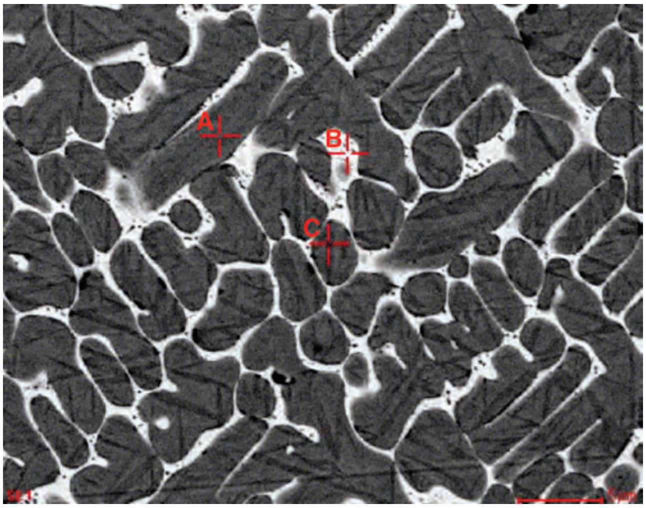

Fig. 8 — Backscattered electron image of the center of the fusion zone of specimen B3-2. EDS analysis of labeled locations is shown in Table 2.

joints. For 2-mm-thick sample A2-2, which was welded with a high heat input, all four specimens exhibited a linear stress-strain curve, the bend strength falling between 311 and 508 MPa, without showing any ductility — Fig. 11A. With the same heat input (achieved using an increased laser power and increased scan speed), 2-mm-thick sample A2-8 exhibited not only a much higher average bend strength (about 826 MPa), but also significant ductility — Fig. 11B. Compared with sample A2-8, a decreased heat input for 2-mm-thick sample A2-9 resulted in three of the specimens to exhibit in low strength (375 MPa average) and one specimen exhibiting high strength and ductility — Fig. 11C.

Figure 11D shows the flexural stress-strain curves of 3-mm-thick specimen B3-2. The maximum and minimum bend strengths were 844.31 MPa and 318.72 MPa with the range of plastic deformation being 0.12 to 0.47 mm.

Table 3 lists the flexural strength of the tested specimens. As can be seen, the maximum bend strength using optimized welding parameters is 970 MPa, and the minimum bend strength is 312 MPa for 2-mm-thick specimens. Even the minimum bend strength compares favorably with reported typical strength for brazed joints.

Except for a few cases in which the specimen contains hot-cracking defects in the fusion zone and the fracture happened in the fusion zone, all bend tested specimens fractured along the fusion boundary on the WC-Co side. An example is shown in Fig. 12, in which the face-bend brittle fracture is shown to have started in the weld fusion zone near the weld toe, propagated across the fusion boundary, and grown parallel to the fusion boundary, but always within the HAZ. The fractography of a typical fractured surface is shown in Fig. 13. In the weld fusion zone portion of the fracture, the fracture mode is intergranular — the fracture separates the interdendritic boundaries and reveals the tips of dendritic arms and the eutectic constituents — Fig. 13A. In the HAZ portion of the fracture, the fracture mode is transgranular — Fig. 13B. At a higher magnification, the fracture in the HAZ showed the undissolved WC particles separated in cleavage mode, and the binding phase separated in microvoid coalescence (dimple) mode, which showed some local ductility — Fig. 14. Near the right center of the micrograph, the arrow points to a cluster of as-solidified dendritic tips, which suggest the existence of mi-

Table 3 — Flexural Bend Strength of the As-Welded Specimens

Specimen ID	Elastic Modulus (GPa)	Yield Strength (MPa)	Tensile Strength (MPa)
A2-2-01	256.94	–	473.05
A2-2-02	247.31	–	508.00
A2-2-03	224.24	–	440.46
A2-2-04	246.98	–	311.60
A2-8-01	249.28	731.71	867.59
A2-8-02	285.97	–	701.21
A2-8-03	267.20	875.96	970.06
A2-8-04	251.47	–	686.20
A2-9-01	272.16	–	365.10
A2-9-02	270.21	842.88	880.01
A2-9-03	271.14	–	417.22
A2-9-04	269.26	–	343.95
B3-2-01	214.21	827.77	827.77
B3-2-02	197.92	–	318.72
B3-2-03	200.35	–	639.71
B3-2-04	191.14	834.70	844.31

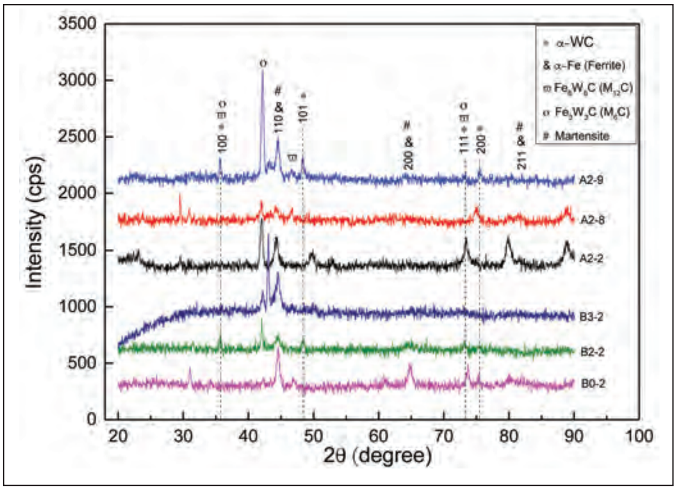

Fig. 9 — XRD results of the weld fusion zones.

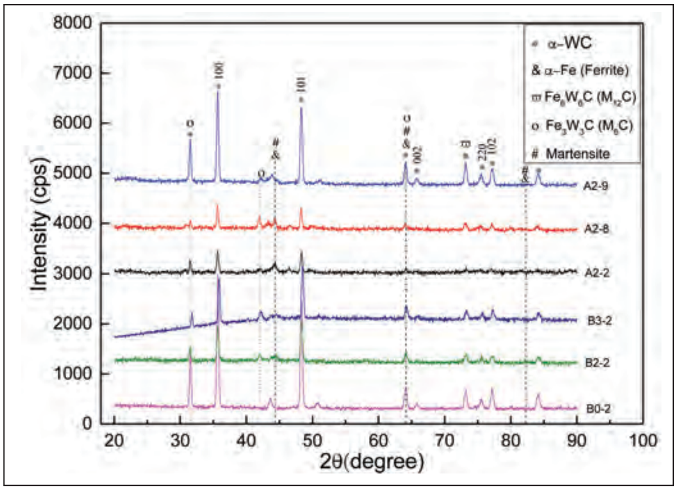

Fig. 10 — XRD results of the HAZs.

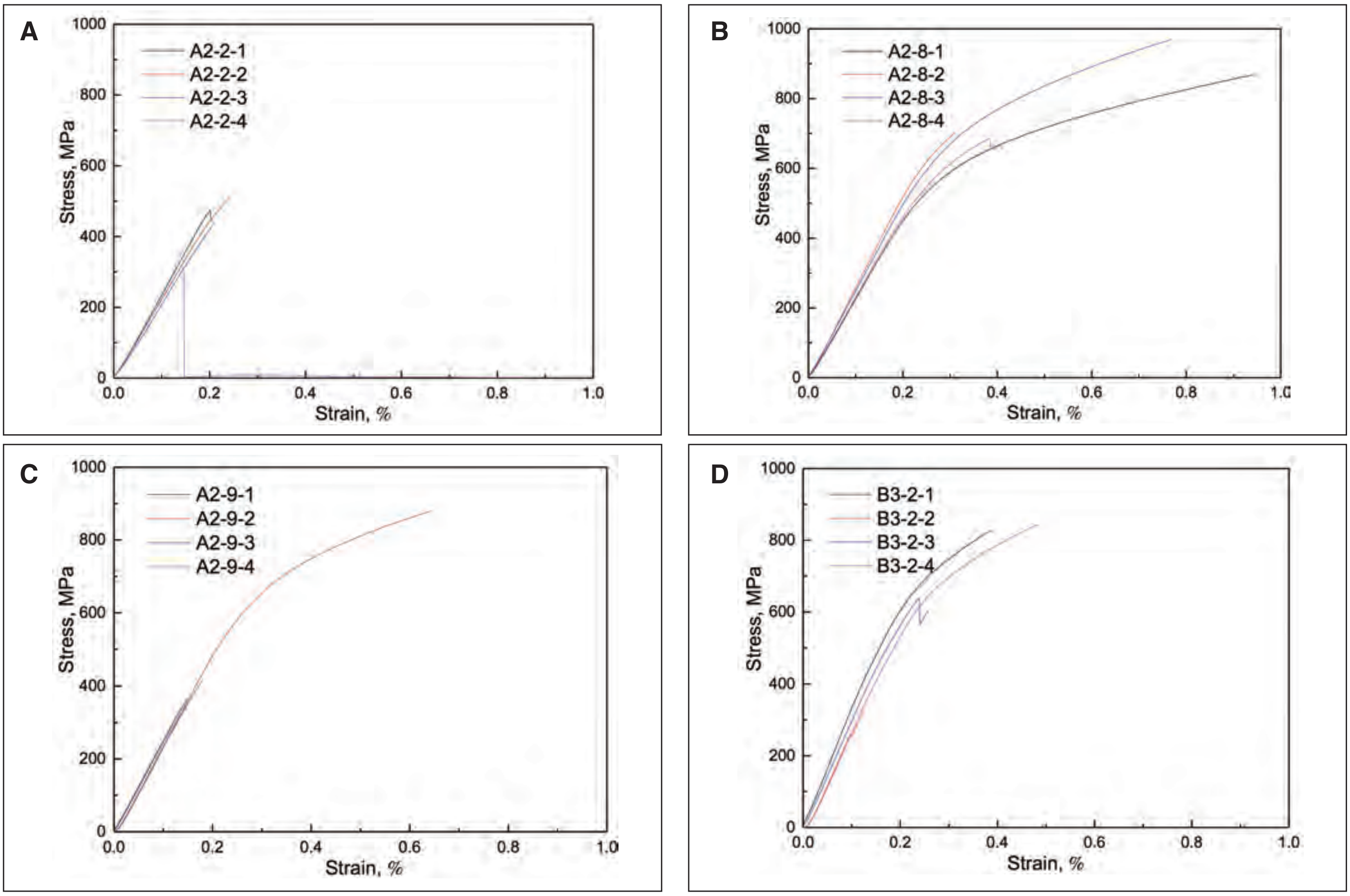

Fig. 11 — Flexural bend strength vs. bend strain curves of the as-welded samples. A — Repeat tests of weld Sample A2-2; B — repeat tests of weld Sample A2-8; C — repeat tests of weld Sample A2-9; and D — repeat tests of weld Sample A3-2. The weld sample identifications are shown in Table 1.

crofissures due to hot tearing near the fusion boundary.

Discussion

The dissimilar materials were fusion welded autogenously, i.e., without adding a filler metal. An analysis of cross-sectional images of joints enabled an estimation of the fusion ratio for the two base materials. Of the welds in this study, on average 20% of the typical fusion zone was melted in from the WC-Co cemented carbide side, and 80% was melted in from the AISI 1045 side. The weld fusion zone chemical composition was thus estimated as 1.2 wt-% C, 0.2 wt-% Si, 0.6 wt-% Mn, 82.2 wt-% Fe, 12.5 wt-% W, wt-% C, and 3.3 wt-% Co. An Fe-W pseudo-binary phase diagram is calcu-

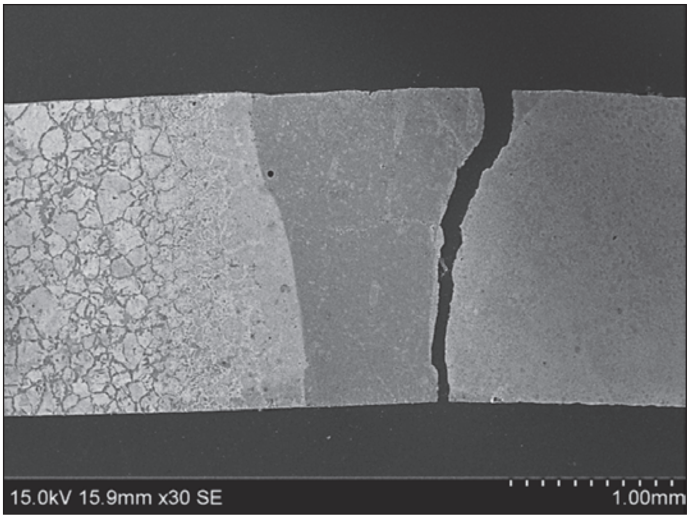

Fig. 12 — A typical face-bend tested specimen showing the fracture propagation path to follow initially the weld toe of the weld fusion zone and then in the HAZ.

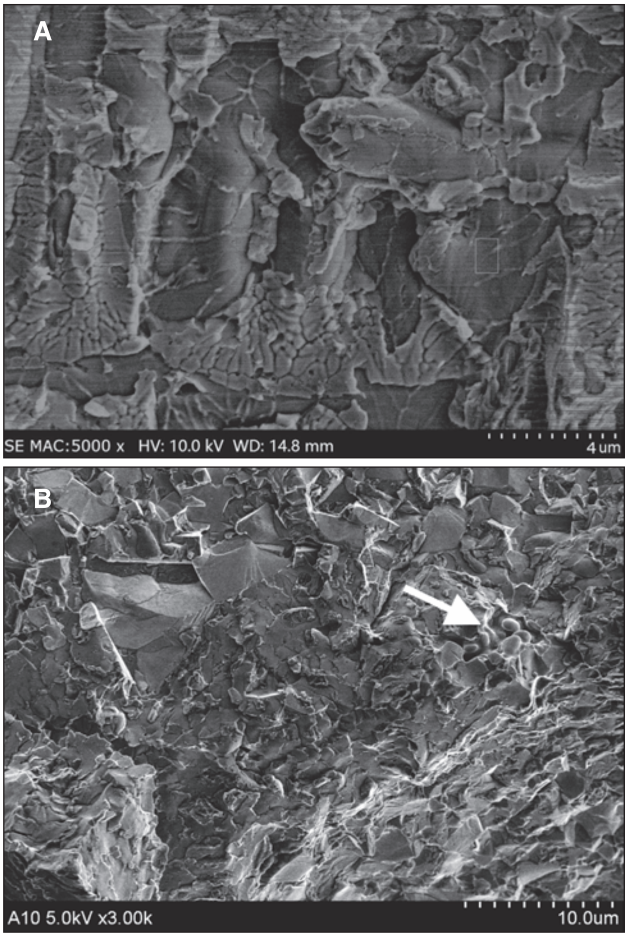

Fig. 13 — Typical bend fracture surface. A — Interdendritic separation in the weld fusion zone; B — transgranular separation in the HAZ.

lated for this composition using the TCFE6 database of *Thermocalc* — Fig. 15. The formation of the fusion zone microstructure upon solidification can be understood using the diagram. For a 12.5%W fusion zone composition, the first solid phase to appear on solidification is the primary dendrites of austenite (g), then there is a multicomponent reaction near 1500 K to form M_6C + µ phase + g eutectic. The µ phase is a Fe-W intermetallic. Upon further cooling, the austenite (g) would transform to a mixture of ferrite (a) + MC carbide + graphite near the 1000 K eutectoid region. Since rapid cooling during laser welding suppresses the diffusional eutectoid reaction, the austenite will transform diffusionlessly to martensite instead. This proposed sequence of transformations seems to be supported by the microstructural, chemical, and phase identifications presented above.

For a composite material, such as WC-Co, the formation of fusion boundary can be complicated because of the different tendencies of dissolution and melting of the two components in the composite. The current case seems to show the fusion boundary to be a boundary region of roughly 30 micrometers thick — Fig. 16. The left edge of the boundary region is the border line distributed on which are partially melted WC carbides. The right edge of the boundary region is indicated by the arrows beyond which there is no evidence for binder melting. In a different specimen, the structure of the fusion boundary region shows eutectic features in the binding phase several grains away from the left weld interface — Fig. 17. The arrows point to the extent in which the eutectic features can still be observed in the binding phase. Therefore, for WC-Co composite, the fusion boundary is a region defined on the higher temperature side by melting of the higher melting point component (WC), and on the lower temperature side by melting of the lower melting point component (Co).

The significance of identification of this fusion boundary region instead of a weld interface is that some earlier observations can now be explained. In the XRD results of both the fusion zone and the HAZ, no original Co binding phase was found. Within this fusion boundary region, the absence of Co can be readily explained by the penetrating Fe and dissolving W that altered the hexagonal Co binding phase to a Fe-based alloy (a cubic crystal system). This proposed boundary region also explains why the HAZ on the WC-Co side is the weakest link for fracture in bend tests. Original more ductile Co was replaced with high-carbon, W- and Fe-enriched brittle eutectic constituents.

TEM analysis is conducted on the HAZ microstructure to verify the dissolution of WC into Co. Figure 18 shows the bright field image of the HAZ of sample A2-8. Two dissolving WC particles are surrounded by the Co binding phase. Zooming in on the point indicated by the arrow, under high-resolution TEM, the WC-Co interface structure is shown in Fig. 19. First, the dissolving WC particle actually turned to W_2C structure at the interface, as observed by other researchers (Ref. 18). The d-spacing of W_2C {1011} planes is 2.229 angstrom. The d-spacing of {1121} planes in the a-Co matrix near the W_2C interface has two values, 2.092 and 2.109 angstrom, with the higher value closer to W_2C. This indicates that through solid solution, the dissolved W and C changed the lattice parameter of Co near the W_2C and a-Co interface.

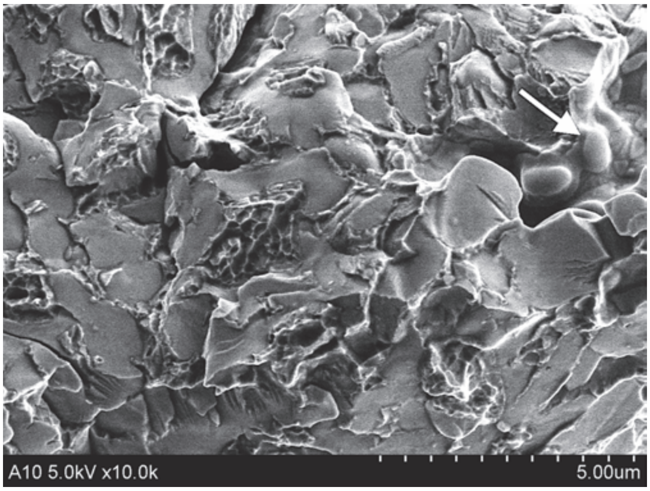

Fig. 14 — Transgranular separation in the HAZ. The WC particles fracture by cleavage; and the binding Co phase fractures by microvoid coalescence (dimple) mode. The arrow points at dendritic tip features that indicate solidification microcracking.

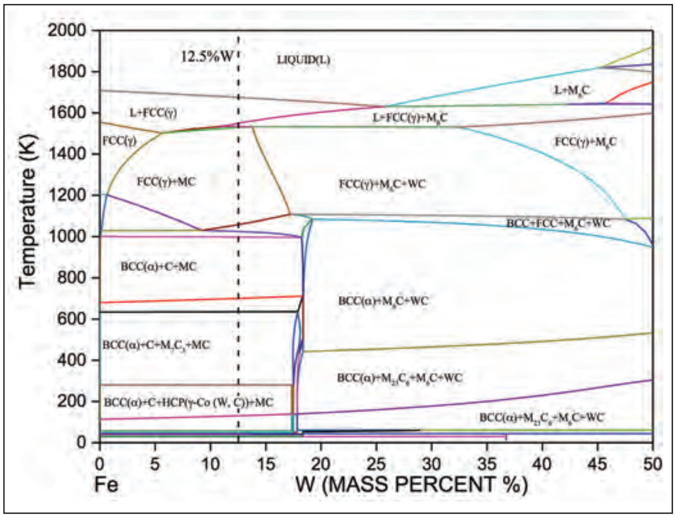

Fig. 15 — Fe-W pseudo-binary phase diagram calculated for a 20% WC-20Co and 80% AISI 1045 mixture.

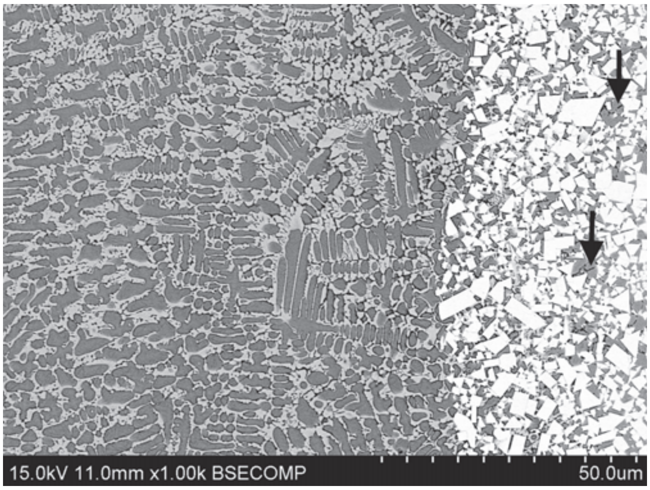

Fig. 16 — The fusion boundary region in the WC-20Co composite. Arrows point to the extent of penetration zone where the binding phase contains dark-contrast, eutectic, constituents.

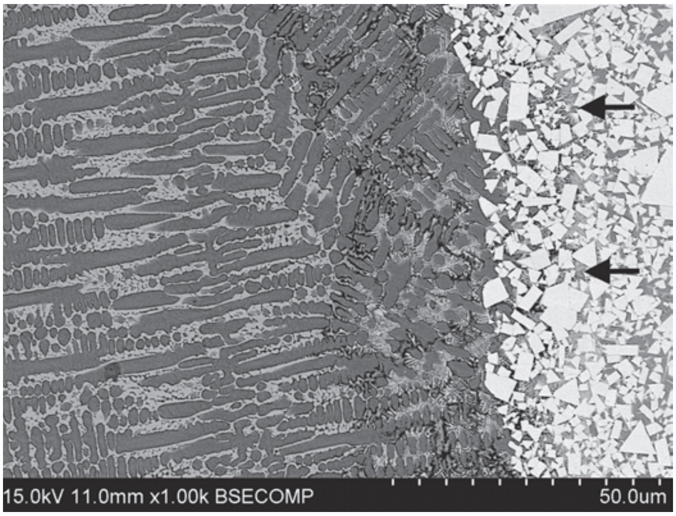

Fig. 17 — A backscattered electron image of the fusion boundary on the WC-20Co side. Arrows point to eutectic features in the binding phase several grains away from the left weld interface.

Conclusions

Three-mm-thick WC-Co and steel dissimilar materials were successfully welded using fiber laser welding. The optimized welding parameters include laser power of 2 kW, scanning speed at 0.96 m/min, and the heat input of 125 J/mm. The flexural bend strength and yield strength of the joints attained 970 MPa and 876 MPa, much higher than that of conventional brazed joints. Brittle fracture during bending occured along the fusion boundary and HAZ on the cemented carbide side, where dissolution of WC and penetration of Fe from the fusion zone are believed to have caused embrittlement at the WC-matrix interfaces.

The joint formation in a WC-Co composite seems to involve the formation of a fusion boundary region that is several WC grains wide (approximately 30 micrometers). The higher temperature border of the fusion boundary region is defined by the melting point of WC. The lower temperature border of the fusion boundary region is defined by the melting point of the Co binding phase.

Acknowledgments

The work was supported in part by the National Natural Science Foundation of China (51475282, 51105240) and "Shu Guang" project of Shanghai Municipal Education Commission and Shanghai Education Development Foundation (13SG54).

References

1. Schroter, K. (Gen. Electric), Hardmetal alloy and the process of making same. U.S. patent, US67176423, 1923.10.31.

2. Fang, Z., Wang, X., Ryu, T., Hwang, K. S., and Sohn, H. Y. 2009. Synthesis, sintering, and mechanical properties of nanocrystalline cemented tungsten carbide — A review. *International Journal of Refractory Metals and Hard Materials* 27(2): 288–299.

3. Zhong, Y., Zhu, H., Shaw, L., and Ramprasad, R. 2011. The equilibrium mor-

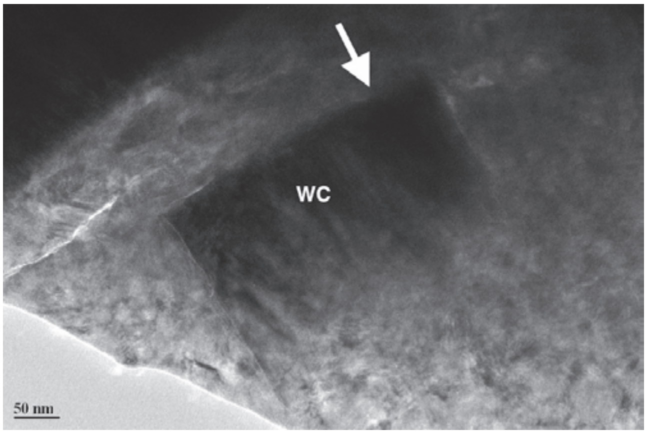

Fig. 18 — TEM bright field image of the WC-Co HAZ.

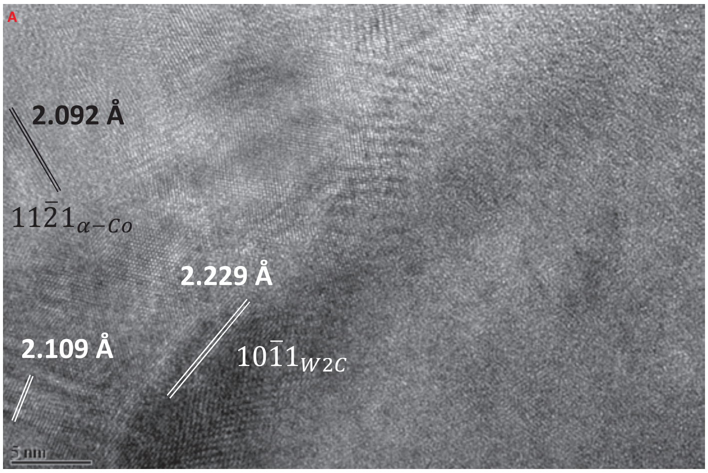

Figure 19 — HRTEM image of the carbide matrix interface indicated by the arrow in Fig. 18.

phology of WC particles — A combined ab initio and experimental study. *Acta Materialia* 59: 3748–3757.

4. Thorsen, K., Fordsmand, H., and Praestgaard, P. 1984. An explanation of wettability problems when brazing cemented carbides. *Welding Journal* 63(10): 308-s to 315-s.

5. Lee, W.-B., Kwon, B.-D., and Jung, S.-B. 2006. Effects of Cr_3C_2 on the microstructure and mechanical properties of the brazed joints between WC-Co and carbon steel. *International Journal of Refractory Metals & Hard Materials* 24(3): 215–221.

6. Zhu, L., Luo, L., Luo, J., Li, J., and Wu, Y. 2012. Effect of electroless plating Ni-Cu-P layer on the wettability between cemented carbides and soldering tins. *Int. Journal of Refractory Metals and Hard Materials* 31(3): 192–195.

7. Rodelas, J., Hilmas, G., and Mishra, R. 2009. Sinterbonding cobalt-cemented tungsten carbide to tungsten heavy alloys. *Int. Journal of Refractory Metals & Hard Materials* 27: 835–841.

8. Andreatta, F., Matesanz, L., Akita, A. H., Paussa, L., Fedrizzi, L., Fugivara, C., Gómez de Salazar, J., and Benedetti, A. 2009. SAE 1045 steel/WC-Co/Ni-Cu-Ni/SAE 1045 steel joints prepared by dynamic diffusion bonding: Microelectrochemical studies in 0.6M NaCl solution. *Electrochimica Acta* 55(2): 551–559.

9. Barrena, M., Gómez de Salazar, J., and Matesanz, L. 2010. Interfacial microstructure and mechanical strength of WC-Co/90MnCrV8 cold work tool steel diffusion bonded joint with Cu/Ni electroplated interlayer. *Materials and Design* 31(7): 3389–3394.

10. Gonda, H., Shirai, Y., Ohashi, O., Yasui, T., and Fukumoto, M. 2011. Application of diffusion bonding to joining between cemented carbides. *Quarterly Journal of the Japan Welding Society* 29(4): 358–363.

11. Choy, K. L. 2003. Chemical vapour deposition of coatings. *Progress in Materials Science* 48: 57–170.

12. Zhao, X., Liu, P., Chen, C., Yang, D., and Kohsuke, T. 2011. Phase formation mechanism at cemented carbide YG30/steel 1045 joints during tungsten-inert-gas arc welding. *Materials Science Forum* 675–677: 901–904.

13. Okita, K., Aritoshi, M., Kuwabara, K., Matsui, M., Takami, C., Kajino, H., and Tsuda, K. 1997. Friction welding of cemented carbide alloy to tool steel. *Welding International* 11(4): 257–263.

14. Tian, N., and Yang, Y. 1996. Study of laser molten welding of cemented carbides and steel. *SPIE* 2888: 185–193.

15. Costa, A., Quintino, L., and Greitmann, M. 2003. Laser beam welding hard metals to steel. *Journal of Materials Processing Technology* 141(2): 163–173.

16. Costa, A., Miranda, R., and Quintino, L. 2006. Materials behavior in laser welding of hard metals to stee. *Materials and Manufacturing Processes* 21(5): 459–465.

17. Barbatti, C., Garcia, J., Liedl, G., and Pyzalla, A. 2007. Joining of cemented carbides to steel by laser beam welding. *Mat.-wiss. u. Werkstofftech.* 38(11): 907–914.

18. Sugiyama, I., Goto, M., Taniuchi, T., Shirase, F., Tanase, T., Okada, K., Ikuhara, Y., and Yamamoto, T. 2011. Blunt corners of WC grains induced by lowering carbon content in WC-12 mass-%Co cemented carbides. *J. Mater. Sci.* 46: 4413–4419.